

¹ Defocus Corrected Large Area Cryo-EM (DeCo-LACE) for Label-Free
² Detection of Molecules across Entire Cell Sections

³

⁴ This manuscript (permalink) was automatically generated from jojoelfe/deco_lace_template_matching_manuscript@a321def
⁵ on June 6, 2022.

⁶ **Authors**

- **Johannes Elferich**  0000-0002-9911-706X ·  jojoelfe RNA Therapeutics Institute, University of Massachusetts Chan Medical School, Worcester, MA, USA; Howard Hughes Medical Institute, Ashburn, VA, USA
- **Giulia Schirotti**  0000-0002-9812-8728 Center for Regenerative Medicine, Massachusetts General Hospital, Boston, MA 02114, USA
- **David Scadden** Center for Regenerative Medicine, Massachusetts General Hospital, Boston, MA 02114, USA; Harvard Stem Cell Institute, Cambridge, MA 02138, USA; Department of Stem Cell and Regenerative Biology, Harvard University, Cambridge, MA 02138, USA
- **Nikolaus Grigorieff**  0000-0002-1506-909X ·  nikogrigorieff RNA Therapeutics Institute, University of Massachusetts Chan Medical School, Worcester, MA, USA; Howard Hughes Medical Institute, Ashburn, VA, USA

¹⁷ **Abstract**

¹⁸ A major goal of biological imaging is localization of biomolecules inside a cell. Fluorescence microscopy can localize biomolecules inside whole cells and tissues, but its ability to count biomolecules and accuracy of the spatial coordinates is limited by the wavelength of visible light. Cryo-electron microscopy (cryo-EM) provides highly accurate position and orientation information of biomolecules but is often confined to small fields of view inside a cell, limiting biological context. In this study we use a new data-acquisition scheme called “Defocus-Corrected Large-Area cryo-EM” (DeCo-LACE) to collect high-resolution images of entire sections (100 – 200 nm thick lamellae) of neutrophil-like mouse cells, representing 1-2% of the total cellular volume. We use 2D template matching (2DTM)

25 to determine localization and orientation of the large ribosomal subunit in these sections. These data provide “maps”
26 of ribosomes across entire sections of mammalian cells. This high-throughput cryo-EM data collection approach
27 together with 2DTM will advance visual proteomics and provide biological insight that cannot be obtained by other
28 methods.

29 **Introduction**

30 A major goal in understanding cellular processes is the knowledge of the amounts, location, interactions, and
31 conformations of biomolecules inside the cell. This knowledge can be obtained by approaches broadly divided into
32 label- and label-free techniques. In label-dependent techniques a probe is physically attached to a molecule of
33 interest that is able to be detected by its strong signal, such as a fluorescent molecule. In label-free techniques,
34 the physical properties of molecules themselves are used for detection. An example for this is proteomics using
35 mass-spectrometry [1]. The advantage of label-free techniques is that they can provide information over thousands
36 of molecules, while label-dependent techniques offer highly specific information for a few molecules. in particular,
37 spatial information is primarily achieved using label-dependent techniques, such as fluorescence microscopy [2].

38 Cryo-electron microscopy (cryo-EM) has the potential to directly visualize the arrangement of atoms that compose
39 biomolecules inside of cells, thereby allowing label-free detection with high spatial accuracy. This has been called
40 “visual proteomics” [3]. Since cryo-EM requires thin samples (<500nm), imaging of biomolecules inside cells is
41 restricted to small organisms, thin regions of cells, or samples that have been suitably thinned. Thinning can
42 be achieved either by mechanical sectioning [4] or by milling using a focused ion beam (FIB) [5]. This complex
43 workflow leads to a low throughput of cryo-EM imaging of cells and is further limited by the fact that at the required
44 magnifications, typical fields of view (FOV) are very small compared to mammalian cells, and the FOV achieved
45 by label-dependent techniques such as fluorescence light microscopy. The predominant cryo-EM technique for
46 the localization of biomolecules of defined size and shape inside cells is cryo-electron tomography [6]. However, the
47 requirement of a tilt series at every imaged location and subsequent image alignment, severely limits the throughput
48 for molecular localization.

49 An alternative approach is to identify molecules by their structural “fingerprint” in single projection using “2D
50 template-matching” (2DTM) [7,8,9]. In this method, a 3D model of a biomolecule is used as a template to find 2D
51 projections that match the molecules visible in the electron micrographs. This method requires a projection search
52 on a fine angular grid, and the projections are used to find local cross-correlation peaks with the micrograph. Since
53 the location of a biomolecule in the z-direction causes predictable aberrations to the projection image, this method
54 can be used to calculate complete 3D coordinates and orientations of a biomolecule in a cellular sample [8].

55 Here we apply 2DTM of the ribosome large subunit (LSU) to conditionally immortalized *mus musculus* (mouse)
56 cell line that gives rise to functional mature neutrophils [10] after thinning using cryo-FIB milling. We chose

57 these cells because genetic defects in the ribosome machinery often leads to hematopoietic disease [11] and direct
58 quantification of ribosome location, number and conformational states in hematopoietic cells could lead to new
59 insight into hematopoietic disease [12]. To increase the amount of collected data and to provide unbiased sampling
60 of the whole lamella, we devised a new data-acquisition scheme, “Defocus-Corrected Large Area Cryo-Electron
61 microscopy” (DeCo-LACE). 2DTM allows us to test whether aberrations caused by large beam-image shifts and
62 highly condensed beams deteriorate the high-resolution signal. We find that these aberrations do not impede LSU
63 detection by 2DTM. The resulting data provide a description of ribosome distribution in an entire lamella, which
64 represent 1-2% of the cellular volume. We find a highly heterogeneous density of ribosomes within the cell. Analysis
65 of the throughput in this method suggests that for the foreseeable future computation will be the bottleneck for
66 visual proteomics.

67 Results

68 2DTM detects large ribosomal subunits in cryo-FIB lamellae of mammalian cells

69 FIB-milled *Saccharomyces cerevisiae* (yeast) cells are sufficiently well preserved to permit localization of 60S ribo-
70 somal subunits with 2DTM [13]. Due to the larger size of mammalian cells compared to yeast cells, it was unclear
71 whether plunge freezing would be adequate to produce vitreous ice across the whole volume of the cell. To test this
72 we prepared cryo-lamellae of mouse neutrophil cells. A low magnification image of a representative lamella clearly
73 shows cellular features consistent with a neutrophile-like phenotype, mainly a segmented nucleus and a plethora
74 of membrane-organelles, corresponding to the granules and secretory vesicles of neutrophils (Fig. [1]A). We then
75 proceeded to acquire micrographs on this lamella with a defocus of 0.5-1.0 m, 30 e⁻/Å²/s exposure and 1.76 Å pixel
76 size. We manually selected multiple locations in the lamella and acquired micrographs using standard low-dose
77 techniques where focusing is performed on a sacrificial area. The resulting micrographs showed smooth bilayered
78 membranes and no signs of crystalline ice (Fig. [1]C,D), indicating successful vitrification throughout the lamella.

79 We used an atomic model of the 60S mouse ribosomal subunit (6SWA) for 2DTM [14]. In a subset of images,
80 the distribution of cross-correlation scores significantly exceeded the distribution expected from images devoid of
81 detectable targets. In the resulting scaled maximum-intensity projections (MIPs), clear peaks with SNR values up
82 to 10 were apparent (Fig. [2 - figure supplement 1]A). Using a threshold criterion to select significant targets (see
83 Methods), we found that in images of cytosolic compartments there were 10-500 ribosomes within one micrograph
84 (Fig. [1]B-E). Notably, we found no targets in areas corresponding to the nucleus (Fig. [1]B) or mitochondria (Fig.
85 1D). In the cytoplasm, we found a highly variable number of targets, only ~ 50 in some exposures (Fig. [1]E) and up
86 to 500 in others (Fig. [1]C). However, it is unclear whether this ten-fold difference in local ribosome concentration
87 is due to technical variation, such as sample thickness, or biological variation. To differentiate between the two
88 we reasoned it was important to not manually choose imaging regions and to collect larger amounts of data. We

89 therefore set out to collect cryo-EM data for 2DTM from mammalian cell lamellae in a high-throughput unbiased
90 fashion.

91 **DeCo-LACE for 2D imaging of whole lamellae**

92 In order to obtain high-resolution data from complete lamellae, we developed a new approach for data collection.
93 This approach uses three key strategies: (1) every electron that exposes a fresh area of the sample is collected on
94 the camera (2) image shift is used to precisely and quickly raster the surface of a lamella and (3) focusing is done
95 without using a sacrificial area (Fig. [2]A).

96 To ensure that every electron exposing a fresh area of the sample is captured by the detector, we adjusted the
97 electron beam size to be entirely contained by the detector area. During canonical low-dose imaging, the microscope
98 is configured so that the focal plane is identical to the eucentric plane of the specimen stage. This leaves the C2
99 aperture out of focus, resulting in ripples at the edge of the beam (Fig. [2]D). While these ripples are low-resolution
100 features that likely do not interfere with 2DTM [7], we also tested data collection under conditions where the C2
101 aperture is in focus (“fringe-free”, Fig. [2]E) [15].

102 We then centered a lamella on the optical axis of the microscope and used the image shift controls of the microscope
103 to systematically scan the whole surface of the lamella in a hexagonal pattern (Fig. [2]A,C). Instead of focusing
104 on a sacrificial area, we determined the defocus from every exposure after it was taken. The defocus was then
105 adjusted based on the difference between desired and measured defocus (Fig. [2]B). Since we used a serpentine
106 pattern for data collection, every exposure was close to the previous exposure, making large changes in the defocus
107 unlikely. Furthermore, we started our acquisition pattern on the platinum deposition edge to make sure that the
108 initial exposure where the defocus was not yet adjusted did not contain any biologically relevant information.

109 We used this strategy to collect data on eight lamellae, four using the eucentric focus condition, hereafter referred to
110 as Lamella_{EUC}, and four using the fringe-free condition, hereafter referred to as Lamella_{FFF}(Fig. [3] A+D, Fig. [4
111 - figure supplement 4]A). We were able to collect data with a highly consistent defocus of 800 nm (Fig. [2]F), both
112 in the eucentric focus and fringe-free focus condition. To ensure that data were collected consistently, we mapped
113 defocus values as a function of the applied image shift (Fig. [3 - figure supplement 1]A). This demonstrated that
114 the defocus was consistent across a lamella, except for rare outliers and in images containing contamination. We
115 also plotted the measured objective astigmatism of each lamella and found that it varies with the applied image
116 shift, becoming more astigmatic mostly due to image shift in the x direction (Fig. [3 - figure supplement 1]B).
117 While approaches exist to correct for this during the data collection [16], we opted to not use these approaches in
118 our initial experiments. We reasoned that because 2DTM depends on high-resolution information, this would be
119 an excellent test of how much these aberration affect imaging.

120 We assembled the tile micrographs into a montage using the image-shift values and the SerialEM calibration followed

121 by cross-correlation based refinement (see Methods). In the resulting montages, the same cellular features visible
122 in the overview images are apparent (Fig. [3]B+E, Fig. [4 - figure supplement 4]B), however due to the high
123 magnification and low defocus many more details, such as the membrane bilayer separation, can be observed (Fig.
124 [3]C+F). For montages collected using the eucentric condition, there are clearly visible fringes at the edges between
125 the tiles (Fig. [3]C), which are absent in the fringe-free focus montages (Fig. [3]F). In our analysis below, we show
126 that these fringes do not impede target detection by 2DTM, making them primarily an aesthetic issue. We also
127 note that the tiling pattern is visible in the montages (Fig. [3]B+E), which we believe is due to the non-linear
128 behavior of the K3 camera since we can observe these shading artifacts in micrographs of a condensed beam over
129 vacuum (Fig. [4 - figure supplement 3]).

130 The montages show membrane vesicles and granules with highly variable sizes and density. We found that a
131 substantial number of granules, which are characterized by higher density inside the the surrounding cytosol [17],
132 seemed to contain a membrane-enclosed inclusion with density similar to the surrounding cytosol (Fig. [4 - figure
133 supplement 4]C) and could therefore be formed by inward budding of the granule membrane. These granules were
134 150-300 nm in diameter and the inclusions were 100-200 nm in diameter. Based on these dimensions the granules are
135 either azurophil or specific granules [17]. To our knowledge, these inclusion have not been described in granulocytes
136 and are further described and discussed below.

137 **2DTM of DeCo-LACE data reveals large ribosomal subunit distribution in cellular cross-sections**

138 In our initial attempts of using 2DTM on micrographs acquired with the DeCo-LACE protocol, we did not observe
139 any SNR peaks above threshold using the large subunit of the mouse ribosome (Fig. [4 - figure supplement 1]A).
140 We reasoned that the edges of the beam might interfere with motion-correction of the movies as they represent
141 strong low-resolution features that do not move with the sample. When we cropped the movie frames to exclude the
142 beam edges, the estimated amount of motion increased (Fig. [4 - figure supplement 1]B), consistent with successful
143 tracking of sample motion. Furthermore, in the motion-corrected average we could identify significant SNR peaks
144 (Fig. [4 - figure supplement 1]B), confirming the high sensitivity of 2DTM to the presence of high-resolution signal
145 preserved in the images by the motion correction. To streamline data processing, we implemented a function in
146 unblur to consider only a defined central area of a movie for estimation of sample motion, while still averaging the
147 complete movie frames (Fig. [4 - figure supplement 1]C). Using this approach, we motion-corrected all tiles in the
148 eight lamellae and found consistently total motion below 1 Å per frame (Fig. [4 - figure supplement 2] A). In some
149 lamellae we found increased motion in the lamella center, which indicates areas of variable mechanical stability
150 within FIB-milled lamellae. In some micrographs we also observed that the beam edges gave rise to artifacts in
151 the MIP and numerous false-positive detections at the edge of the illuminated area (Fig. [4 - figure supplement
152 1]D). A similar phenomenon was observed on isolated “hot” pixels in unilluminated areas. To overcome this issue
153 we implemented a function in unblur to replace dark areas in the micrograph with Gaussian noise (see Methods),

154 with mean and standard deviation matching the illuminated portion of the micrograph (Fig. [4 - figure supplement
155 1]D+E). Together, these pre-processing steps enabled us to perform 2DTM on all tiles of the eight lamellae.

156 We used the tile positions to calculate the positions of the detected LSUs in the lamellae (Fig. [4]A, Fig. [5]A).
157 Overlaying these positions of the lamellae montages reveals LSU distribution throughout the FIB-milled slices of
158 individual cells. Consistent with prior observations imaging selected views in yeast [13], organelles like the nucleus
159 and mitochondria only showed sporadic targets detected with low SNRs, consistent with the estimated false-positive
160 rate of one per tile. For each detected target we also calculated the Z positions from the individual estimated defocus
161 and defocus offset for each tile. When viewed from the side, the ribosome positions therefore show the slight tilts
162 of the lamellae relative to the microscope frame of reference (Fig. [4]B, Fig. [5]B). Furthermore, the side views
163 indicated that lamellae were thinner at the leading edge. Indeed, when plotting the transmitted beam intensities in
164 individual tiles as a function of beam image-shift, we observed substantially higher intensities at the leading edge
165 (Fig. [4 - figure supplement 2]B), which in energy-filtered TEM indicates a thinner sample [18]. Even though we
166 prepared the lamellae with the “overtilt” approach [19], this means that LSU densities across the lamellae can be
167 skewed by a change in thickness, and better sample preparation methods are needed to generate more even samples.

168 Close inspection of the LSU positions in the lamellae revealed several interesting features. LSUs could be seen
169 associating with membranes, in patterns reminiscent of the rough endoplasmic reticulum (Fig. [4]C, Fig. [5]C) or
170 the outer nuclear membrane (Fig. [4]D). We also observed LSUs forming ring-like structures (Fig. [4]E), potentially
171 indicating circularized mRNAs [20]. While ribosomes were for the most part excluded from the numerous granules
172 observed in the cytoplasm, in some cases we observed clusters of LSUs in the inclusions of double-membraned
173 granules described earlier (Fig. [4]F, Fig. [5]D,E). It is, in principle, possible that these targets are situated above
174 or below the imaged granules, since the granule positions in z cannot be determined using 2D projections. However,
175 in the case of Fig. [5]E, the detected LSUs span the whole lamella in the z direction (Fig. [5]F), while positions
176 above or below a granule would result in LSUs situated exclusively at the top or bottom of the lamella. This is
177 consistent with the earlier hypothesis that the inclusions are of cytoplasmic origin.

178 Does DeCo-LACE induce aberrations that affect 2DTM?

179 Within the eight lamellae we found different numbers of detected targets, ranging from 1089 to 6433 per lamella (Fig.
180 [6]A). Lamella_{EUC} 1 had the most detected targets, but also has the largest surface area and contained cytoplasm
181 from two cells. Lamella_{FFF} 4 had the fewest detected targets, but this particular lamella was dominated by a
182 circular section of the nucleus, with only small pockets of cytoplasm (Fig. [4 - figure supplement 4]). In an attempt
183 to normalize for these differences in area containing cytoplasm, we compared the number of detected targets per
184 tile in tiles that contained more than one target, which should exclude tiles with non-cytosolic content (Fig. [6]B).
185 While this measure had less variability, there were still differences. Lamella_{EUC} 4 had not only the fewest targets,

186 but also the lowest density, which could be due to this lamella being the thinnest, or due to it sectioning the cell
187 in an area with a lower concentration of ribosomes. Lamella_{FFF} 3 had a substantially higher number of ribosomes
188 per tile. Since all of these lamellae were made from a cell-line under identical conditions, this underscores the
189 necessity to collect data from large numbers of lamellae to overcome the inherent variability. When comparing the
190 distribution of scores between lamellae, we found them to be fairly comparable with median SNRs ranging from
191 8.7 to 9.7 (Fig. [6]C). Lamella_{EUC} 1 had slightly lower scores compared to the rest, potentially due to its large
192 size and connected mechanical instability during imaging. Overall, we did not observe differences in the number or
193 SNR of detected targets between eucentric or fringe-free illumination conditions that were bigger than the observed
194 inter-lamella variability.

195 Since the SNR values of 2DTM are highly sensitive to image quality, we reasoned we could use them to verify
196 that DeCo-LACE does not introduce a systematic loss of image quality. We considered non-parallel illumination
197 introduced by the unusually condensed beam and uncharacterized aberrations near the beam periphery. When
198 plotting the SNR values of detected targets in all eight lamellae as a function of their location in the tiles, we found
199 uniformly high SNR values throughout the illuminated areas for both eucentric and fringe-free focus illumination,
200 demonstrating that both illumination schemes are suitable for DeCo-LACE (Fig. [6]D).

201 We also wondered whether large image shifts would lead aberration due to astigmatism or beam tilt [16]. We
202 reasoned that if that was the case the number of detected targets should be highest in the center of the lamella
203 where the applied beam image-shift is 0. Instead, we observed that in both eucentric and fringe-free focus conditions
204 more targets were detected at the “back” edge of the lamella (Fig. [6]E). This may be due to the center of the
205 cell being predominantly occupied by the nucleus, despite its segmentation in neutrophil-like cells. The increase in
206 matches at the “back” of the lamellae compared to the “front” can also be explained by the thickness gradient of the
207 lamellae (Fig. [4 - figure supplement 2]B, Fig. [4]B, Fig. [5]B). In addition, aberrations would be expected to cause
208 average 2DTM SNRs to be higher when beam-image shift values are small. Instead, we found that SNRs were
209 on average the highest at the “front” edge of the lamellae, presumably due to the thinner sample. We therefore
210 conclude that factors other than beam image-shift or beam condensation aberrations are limiting 2DTM SNRs,
211 predominantly the thickness of the lamellae.

212 Computation is the bottleneck of visual proteomics

213 All lamellae described above were derived from a clonal cell line under identical condition and thinned with the
214 same parameters. This means that the substantial variability of detected targets between the lamellae must be due
215 to technical variability, including area, thickness, mechanical stability, and location of the section within the cell.
216 We therefore predict that further studies that want to draw quantitative and statistically relevant conclusions about
217 the number and location of molecules under different experimental conditions, will require collection of orders of

218 magnitude more data than in this study to gain enough statistical power given this variability. The samples used
219 were prepared in two 24 h sessions on a FIB/SEM instrument, and imaging was performed during another two
220 24h session on the TEM microscope. Inspections of the timestamps of the raw data files revealed that the milling
221 time per lamella was ~30 minutes and TEM imaging was accomplished in ~10 seconds per tile or 90 minutes for
222 a ~ 6x6 m lamella. Processing of the data, however, took substantially longer. Specifically, 2DTM of all tiles
223 took approximately one week per lamella on 32 Nvidia A6000 GPUs. Computation is therefore a bottleneck in our
224 current workflow, and further optimizations of the algorithm may be necessary increase throughput. Alternatively,
225 this bottleneck could be reduced by increasing the number of processing units.

226 Discussion

227 In this study we developed an approach to image entire cellular cross-section using cryo-EM at high enough resolution
228 to allow for 2DTM detection of the LSU. The two main advantages compared to previous approaches are a high
229 throughput of imaging and the biological context for detected molecules. The requirement to increase throughput in
230 cryo-EM data collection of cellular samples has been recognized in the recent literature. Most approaches described
231 so far are tailored towards tomography. Peck et al. [21] and Yang et al. [22] developed approaches to increase the
232 FOV of tomogram data-collection by using a montaging technique. Peck et al. used a similar “condensed-beam”
233 approach as described here. However, the montages are substantially smaller in scope, covering carbon film holes
234 of 2 um diameter. Bouvette et al. [23] and Eisenstein et al. [24] are using beam image-shift to collect tilt-series in
235 multiple locations in parallel to increase throughput. However, none of these approaches provide the full coverage
236 of a cellular cross-section that can be achieved using DeCo-Lace.

237 Since we observed substantial variation in LSU density within and between lamellae, visual proteomics studies that
238 use cryo-EM to establish changes in molecular organization within cells will require orders of magnitude more data
239 than used in this study. One milestone would be to image enough data to represent one cellular volume, which
240 for a small eukaryotic cells requires imaging approximately 100 lamella. While data collection throughput on the
241 TEM is fundamentally limited by the exposure time, this amount of data could be collected within 12 hours by
242 improving the data acquisition scheme to perform all necessary calculations in parallel with actual exposure of the
243 camera. Sample preparation using a FIB/SEM is also currently a bottleneck, but preparation of large lamellae with
244 multiple cellular cross-sections using methods like WAFFLE [25] might allow sufficient throughput. As stated in
245 the results, at least for 2DTM computation will remain challenging and approximately 17,000 GPU hours would
246 be required for a 100 lamellae dataset.

247 As described in [7] the 2DTM SNR threshold for detecting a target is chosen to result in one false positive detection
248 per image searched. We would therefore expect to find one false positive detection per tile. We reasoned that the
249 large nuclear area imaged by DeCo-Lace could be used to test whether this assumption is true. In the 670 tiles

250 containing exclusively nucleus (as manually annotated from the overview image) we detected 247 targets, making
251 the false-positive rate more than twofold lower than expected. Since earlier work shows that 2DTM with the LSU
252 can produce matches to nuclear ribosome biogenesis intermediates [13], this could even be an overestimate of the
253 false-positive rate. This suggests that the detection threshold could be even lower, which is an area of ongoing
254 research.

255 We found that even though we used beam image-shift extensively (up to 7 um), we did not see substantially reduced
256 2DTM SNR values in tiles acquired at high beam image-shift compared to tiles acquired with low or no beam image-
257 shift. This is in contrast to reports in single-particle analysis (SPA) [26] where the induced beam tilt substantially
258 reduced the resolution if it was not corrected during processing. It is possible that 2DTM is less sensitive to beam-
259 tilt aberrations, since the template is free of any aberration and only the image is distorted, while in SPA the beam
260 tilt will affect both the images and the reconstructed template.

261 As mentioned in the results, we found a consistent shading artifact pattern in our montages, that we believe is the
262 result of non-linear behavior of the K3 camera. Indeed, when we average images with a condensed beam taken
263 over vacuum we found in both focus conditions a consistent background pattern with a brighter region on the
264 periphery of the illuminated area (Fig [4 - figure supplement 3]). This might be caused by dynamic adjustment
265 of the internal camera counting threshold which expects columns of the sensor to be evenly illuminated as is the
266 case for SPA applications. Since the signal of this pattern has mainly low-resolution components it is unlikely to
267 affect 2DTM. However, it highlights that the non-linear behavior of the camera has to be taken into account when
268 imaging samples with strongly varying density and unusual illumination schemes.

269 We observed granules containing a vesicle of putative cytosolic origin. We speculate that upon degranulation, the
270 process in which granules fuse with the plasma membrane, these vesicles would be released into the extracellular
271 space. The main types of extracellular vesicles of this size are exosomes, up to 100 nm large vesicles derived
272 from fusion of multivesicular bodies with the plasma membrane, and microvesicles, which are derived from direct
273 budding of the plasma membrane [27]. We suggest that granulocytes could release a third type of extracellular
274 vesicle, granule-derived vesicles (GDV), into the extracellular space. 2DTM showed that a subset of GDVs can
275 contain ribosomes (Fig. [4]F, Fig. [5]D,E). This could indicate that these vesicles are transporting translation-
276 capable mRNAs, as has been described for exosomes [28]. Further studies will be necessary to confirm the existence
277 of GDVs in granulocytes isolated from mammals and to understand their functional significance.

278 Materials and Methods

279 Grid preparation

280 ER-HoxB8 cells were maintained in RPMI medium supplemented with 10% FBS, penicillin/streptomycin, SCF,
281 and estrogen [10] at 37 °C and 5% CO2. 120 h prior to grid preparation, cells were washed twice in PBS and

282 cultured in the same medium except without estrogen. Differentiation was verified by staining with Hoechst-dye
283 and inspection of nuclear morphology. Cells were then counted and diluted to $1 \cdot 10^6$ cells/ml. Grids (either 200
284 mesh copper grids, with a silicone-oxide and 2 μm holes with a 2 μm spacing or 200 mesh gold grids with a thin
285 gold film and 2 μm holes in 2 μm spacing) were glow-discharged from both sides using a 15 mA for 45 s. 3.5 μl
286 of cell suspension was added to grids on the thin-film side and grids were blotted from the back side using a GP2
287 cryoplunger (Leica) for 8 s and rapidly plunged into liquid ethane at -185 °C.

288 **FIB-milling**

289 Grids were loaded into an Aquilos 2 FIB/SEM (Thermo Fisher) instrument with a stage cooled to -190 °C. Grids
290 were sputter-coated with platinum for 15 s at 45 mA and then coated with a layer of platinum-precursor by opening
291 the GIS-valve for 45 s. An overview of the grid was created by montaging SEM images and isolated cells at the
292 center of gridsquares were selected for FIB-milling. Lamellae were generated automatically using the AutoTEM
293 software (Thermo Fisher), with the following parameters:

- 294 • Milling angle: 20°
- 295 • Rough milling: 3.2 μm thickness, 0.5 nA current
- 296 • Medium milling: 1.8 μm thickness, 0.3 nA current, 1.0° overtilt
- 297 • Fine milling: 1.0 μm thickness, 0.1 nA current, 0.5° overtilt
- 298 • Finer milling: 700 nm thickness, 0.1 nA current, 0.2° overtilt
- 299 • Polish 1: 450 nm thickness, 50 pA current
- 300 • Polish 2: 200 nm thickness, 30 pA current

301 This resulted in 6-10 μm wide lamella with 150-250 nm thickness as determined by FIB-imaging of the lamella
302 edges.

303 **Data collection**

304 Grids were loaded into a Titan Krios TEM (Thermo Fisher) operated at 300 keV and equipped with a BioQuantum
305 energy filter (Gatan) and K3 camera (Gatan). The microscope was aligned using a cross-grating grid on the stage.
306 Prior to each session, we carefully performed the “Image/Beam” calibration in nanoprobe. We set the magnification
307 to a pixel size of 1.76 Å and condensed the beam to ~ 900 nm diameter, resulting in the beam being completely
308 visible on the camera. To establish fringe-free conditions, the “Fine eucentric” procedure of SerialEM [29] was used
309 to move a square of the cross-grating grid to the eucentric position of the microscope. The effective defocus was
310 then set to 2 μm , using the “autofocus” routine of SerialEM. The objective focus of the microscope was changed
311 until no fringes were visible. The stage was then moved in Z until images had an apparent defocus of 2 μm . The
312 difference in stage Z-position between the eucentric and fringe-free conditions was used to move other areas into

313 fringe-free condition.

314 Low magnification montages were used to find lamellae and lamellae that were sufficiently thin and free of con-
315 tamination were selected for automated data collection. Overview images of each lamella were taken at 2250x
316 magnification (38 Å pixel size). The corners of the lamella in the overview image were manually annotated in
317 SerialEM and translated into beam image-shift values using SerialEM’s calibration. A hexagonal pattern of beam
318 image-shift positions was calculated that covered the area between the four corners in a serpentine way, with a
319 $\sqrt{3} \cdot 425$ nm horizontal spacing and $3/4 \cdot 850$ nm vertical spacing. Exposures were taken at each position with a 30
320 $e^-/\text{\AA}^2$ total dose. After each exposure, the defocus was estimated using the ctffind function of SerialEM and the
321 focus for the next exposure was corrected by the difference between the estimated focus and the desired defocus of
322 800 nm. Furthermore, after each exposure the deviation of the beam from the center of the camera was measured
323 and corrected using the “CenterBeamFromImage” command of SerialEM.

324 After data collection, a 20 s exposure at 2250x magnification of the lamella at 200 m defocus was taken for
325 visualization purposes. A Python script implementing this procedure is available at [Link to repo].

326 DeCo-LACE data processing

327 An overview of the data analysis pipeline is shown in Fig. 7.

328 **Pre-processing** Motion-correction, dose weighting and other preprocessing as detailed below was performed
329 using *cisTEM* [30]. To avoid influence of the beam-edge on motion-correction, only a quarter of the movie in the
330 center of the camera was considered for calculation of the estimated motion. After movie frames were aligned and
331 summed, a mask for the illuminated area was calculated by lowpass filtering the image with a 100 Å resolution
332 cutoff, thresholding the image at 10% of the maximal value and then lowpass filtering the mask again with a 100 Å
333 resolution cutoff to smooth the mask edges. This mask was then used to select dark areas in the image and fill the
334 pixels with Gaussian noise, with the same mean and standard deviation as the illuminated area. A custom version
335 of the unblur program [31] implementing this procedure is available at [link to decolace branch]. During motion
336 correction images were resampled to a pixel size of 1.5 Å. The contrast-transfer function (CTF) was estimated using
337 ctffind [32], searching between 0.2 and 2 m defocus.

338 **2DTM** The search template was generated from the atomic model of the mouse LSU (PDB 6SWA, exluding the
339 Epb1 subunit) using the cryo-EM simulator implemented in *cisTEM* [33]. The match_template program [9] was
340 used to search for this template in the movie-aligned, exposure-filtered and masked images, using a 1.5° angular
341 step in out-of-plane angles and a 1.0° angular step in-plane. 11 defocus planes in 20 nm steps centered around the
342 ctffind-determined defocus were searched. Targets were defined as detected when their matches with the template
343 produced peaks with a singal-to-noise ratio (SNR) above a threshold of 7.75, which was chosen based on the

344 one-false-positive-per-tile criterion [7].

345 **Montage assembly** The coordinates of each tile i , \mathbf{c}_i [2D Vector in pixels] were initialized using beam image-shift
346 of the tile, \mathbf{b}_i [2D Vector in m], and the ISToCamera matrix \mathbf{IC} , as calibrated by SerialEM:

$$\mathbf{c}_i = \mathbf{IC} \cdot \mathbf{b}_i$$

347 A list of tile pairs i, j that overlap were assembled by selecting images where $|\mathbf{c}_i - \mathbf{c}_j| < D_{Beam}$. In order to calculate
348 the precise offset between tiles i and j , $\mathbf{r}_{i,j}$, we calculated the cross-correlation between the two tiles, masked to
349 the overlapping illuminated area using the scikit-image package [34] was used to calculate refined offsets . The
350 coordinates \mathbf{c}_i were then refined by a least-square minimization against $\mathbf{r}_{i,j}$:

$$\min_{\mathbf{c}} \sum_{pairs} (\mathbf{r}_{i,j} - (\mathbf{c}_i - \mathbf{c}_j))^2$$

351 using the scipy package [35]. The masked cross-correlation and the least-square minimization was repeated once
352 more to arrive at the final tile alignment.

353 The x,y coordinates of target n detected by 2DTM in the tile i , $\mathbf{m}_{n,i}^T$, was transformed into the montage frame by
354 adding the coordinate of the tile.

$$\mathbf{m}_n^M = \mathbf{m}_{n,i}^T + \mathbf{c}_i$$

355 The z coordinate of each target was calculated as the sum of the defocus offset for the target, the estimated defocus
356 of the tile, and the nominal defocus of the microscope when the tile was acquired.

357 Images were rendered using UCSF ChimeraX [36] using a custom extension to render 2DTM results available
358 at [<https://github.com/jojoelfe/tempest>]. The Python scripts used for data processing are available under
359 [https://github.com/jojoelfe/deco_lace_template_matching_manuscript].

360 Acknowledgments

361 The authors would like to thank Bronwyn Lucas, Carsten Sachse, and Chen Xue for helpful suggestions and careful
362 reading of the manuscript. Data was collected at the UMass Chan medical School CryoEM core with help by
363 Kankang song, Christna, and Chen Xue.

364 **Data availability**

365 Cryo-EM movies, motion-corrected images and template matching results have been deposited in EMPIAR under
366 accession code [CODE]. The custom cisTEM version is available here [] until features have been integrated into a
367 cisTEM release. The ChimeraX extension for rendering is available here []. This manuscript was prepared using the
368 manubot package [@ cite]. Custom python scripts and all files necessary for manuscript generation are available
369 here [].

370 **Figures**

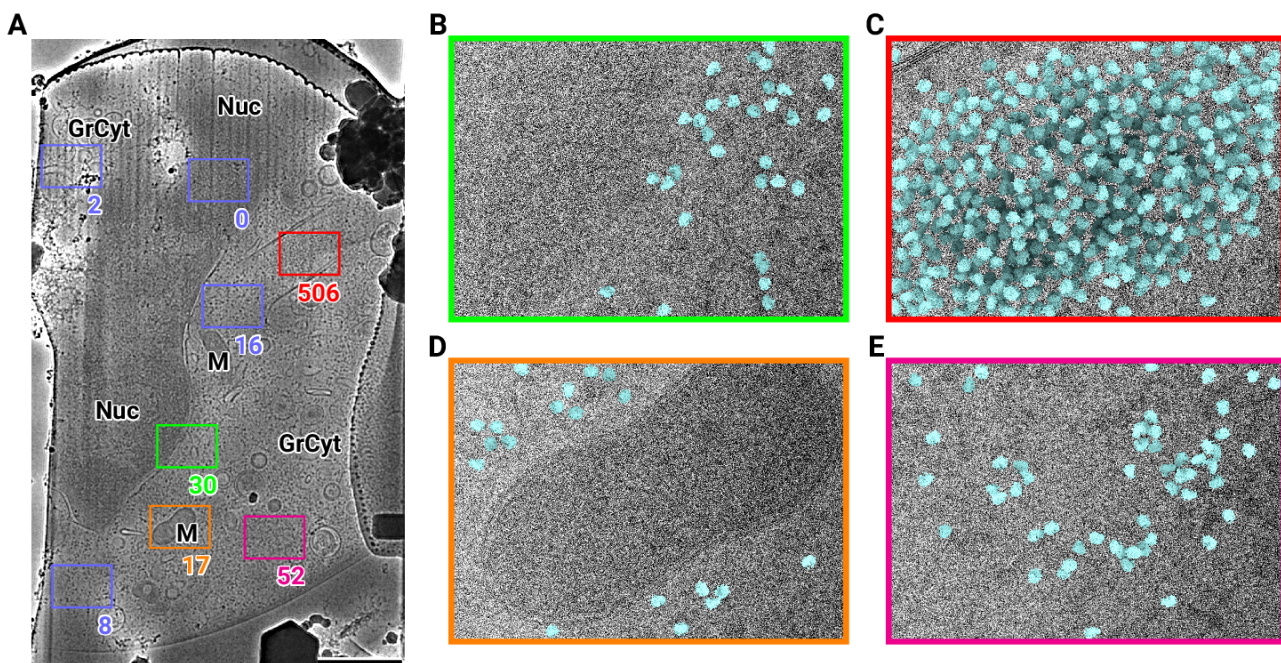


Figure 1: 2D template matching of the large subunit of the ribosome in fib-milled neutrophil-like cells (A) Overview image of the lamella. Major cellular regions are labeled, as Nucleus (Nuc), Mitochondria (M), and granular cytoplasm (GrCyt). FOVs where high-magnification images for template matching were acquired are indicated as boxes with the number of detected targets indicated on the bottom right. FOVs displayed in Panels B-E are color-coded. Scalebar corresponds to 1 μm. (B-E) FOVs with projection of detected LSUs shown in cyan. (B) Perinuclear region, the only detected targets are in the cytoplasmic half. (C) Cytoplasmic region with high density of ribosomes (D) Mitochondrion, as expected there are only detected LSUs in the cytoplasmic region (E) Cytoplasm, with low density of ribosomes.

371 **References**

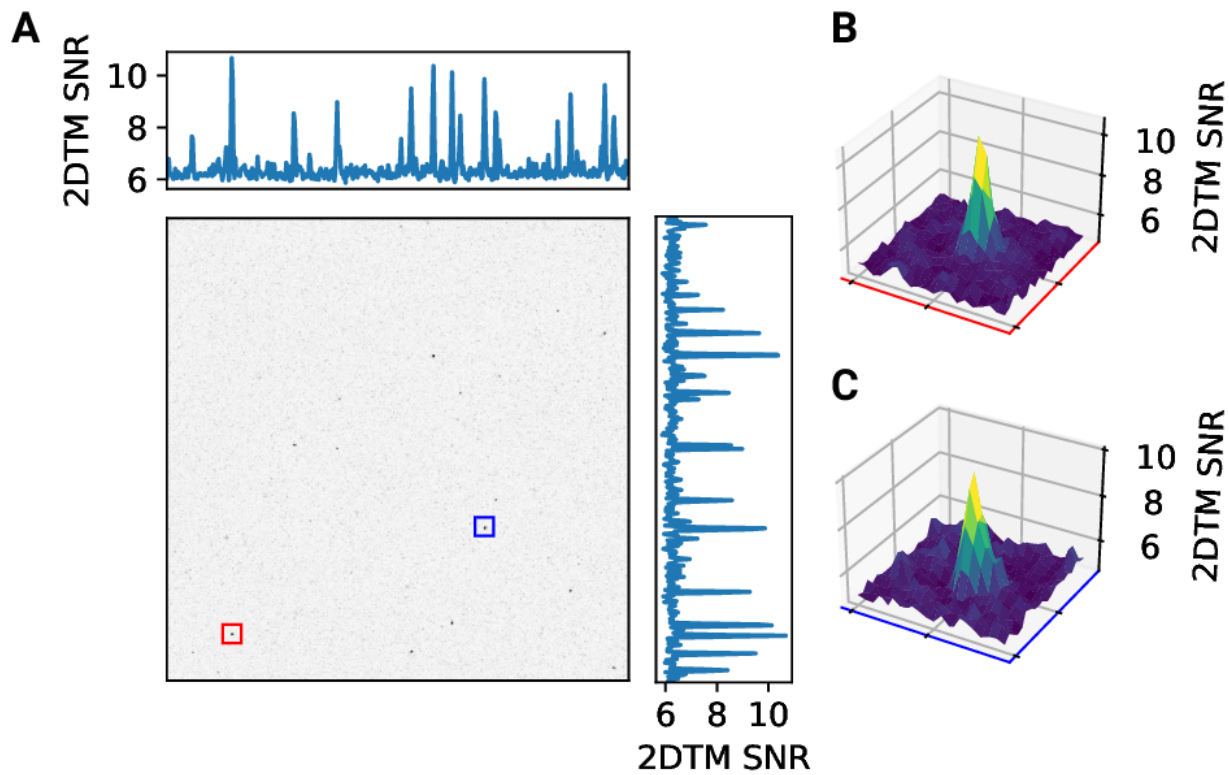


Figure 2 - figure supplement 1: 2D template matching of the large subunit of the ribosome in fib-milled neutrophil-like cells (A) Maximum intensity projection (MIP) cross-correlation map of micrograph shown in Figure 1 (B+C) 3D plot of MIP regions indicated by color boxes in Panel A

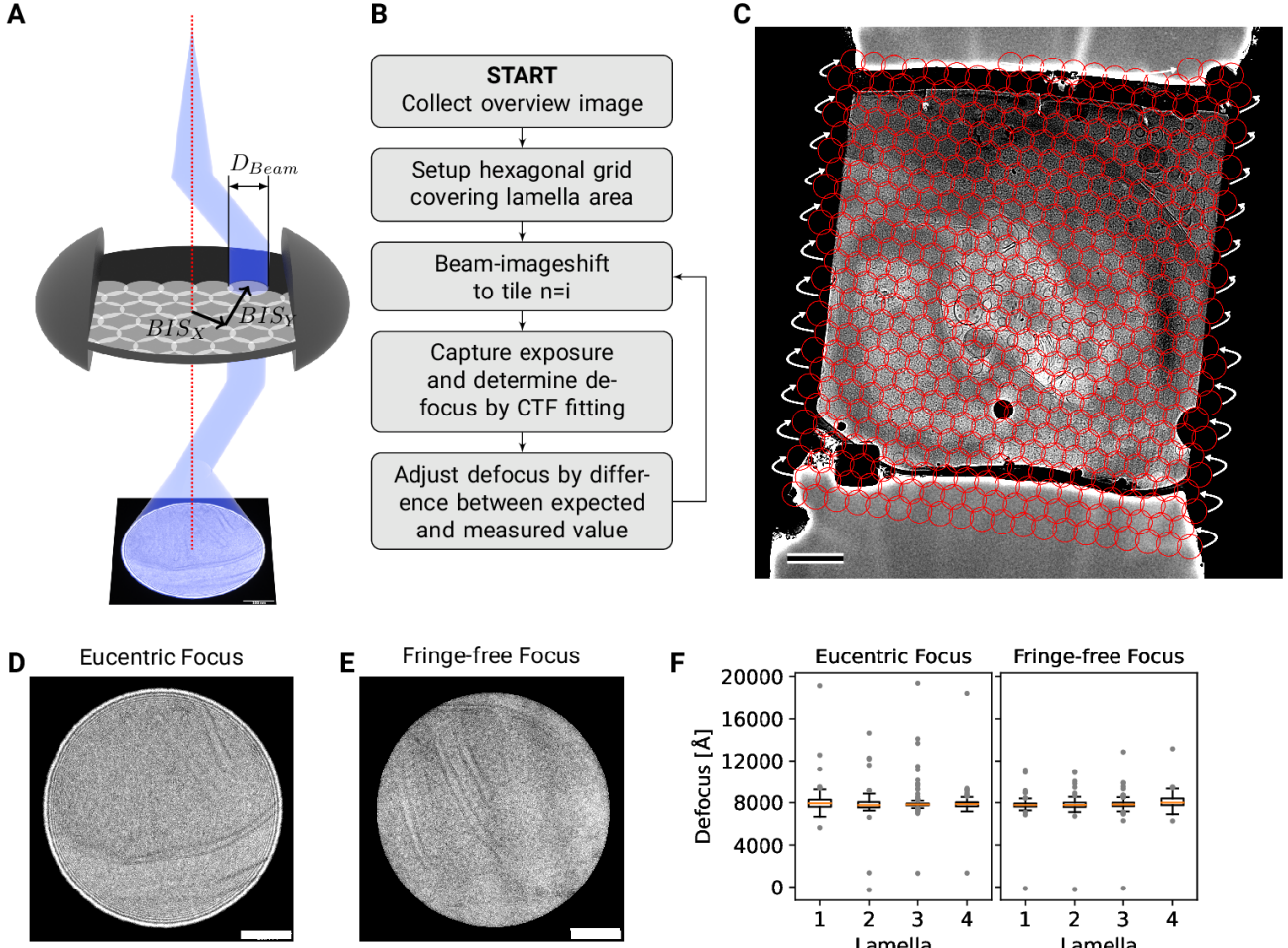


Figure 2: DeCo-LACE approach (A) Graphic demonstrating the data-collection strategy for DeCo-LACE. The electron beam is condensed to a diameter D_{Beam} that allows captured of the whole illuminated area on the camera. Beam-image shift along X and Y (BIS_X, BIS_Y) is used to scan the whole lamella (B) Diagram of the collection algorithm (C) Example overview image of a lamella with the designated acquisition positions and the used beam diameter indicated with red circles. Scalebar corresponds to 1 m. (D+E) Representative micrographs taken with a condensed beam at eucentric focus (D) or fringe-free focus (E). Scalebar corresponds to 100 nm. (F) Boxplot of defocus measured by ctffind of micrographs taken by the DeCo-Lace approach on four lamellae images at eucentric focus and four lamellae imaged with fringe-free focus.

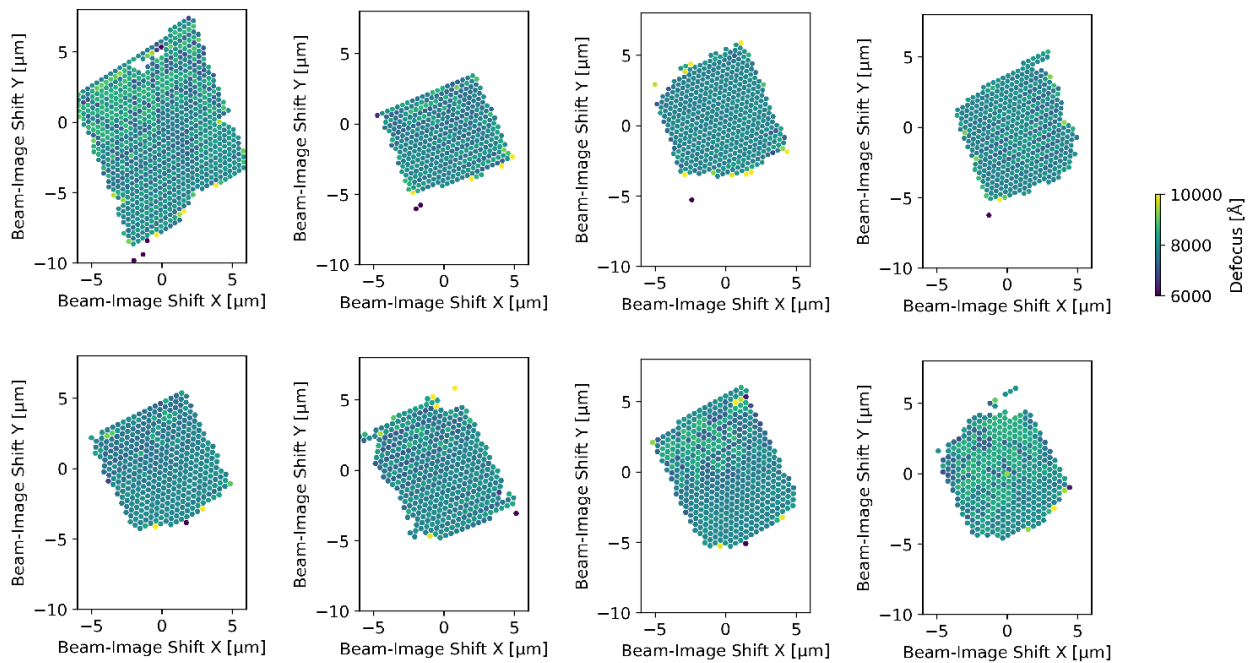
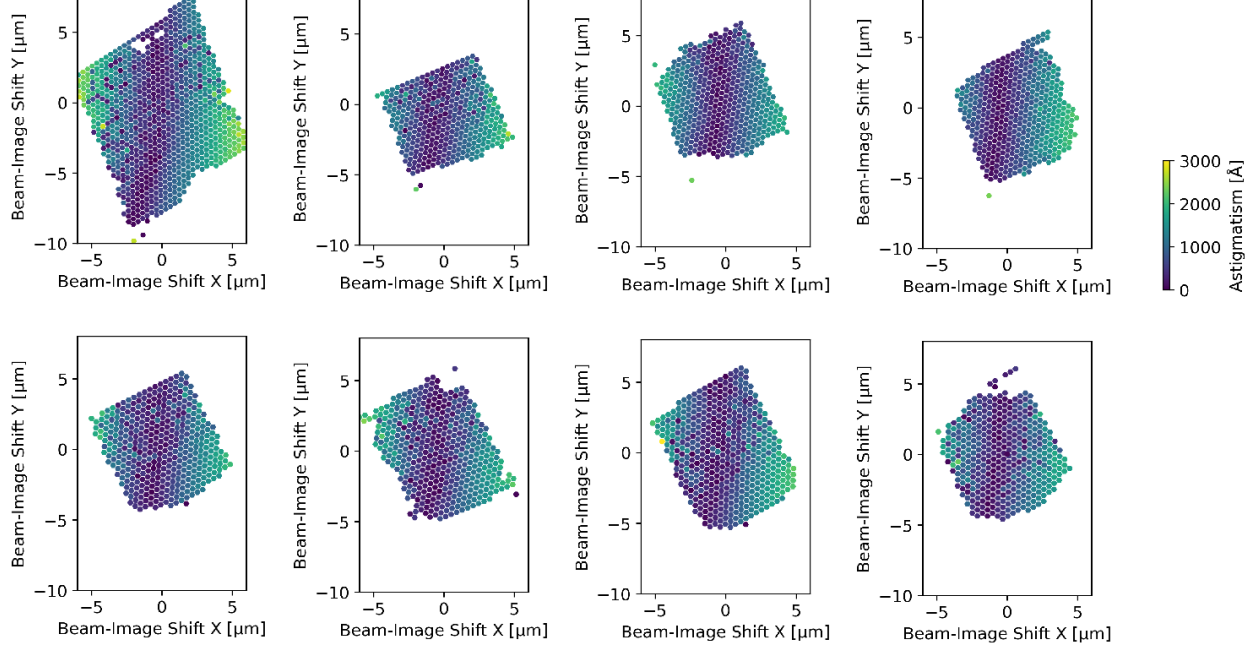
A**B**

Figure 3 - figure supplement 1: Defocus estimation of individual tiles of DeCo-Lace montages (A) Defocus values of individual micrographs taken using the DeCo-Lace approach plotted as a function of the beam image-shift values. (B) Defocus astigmatism of individual micrographs taken using the DeCo-Lace approach plotted as a function of the beam image-shift values.

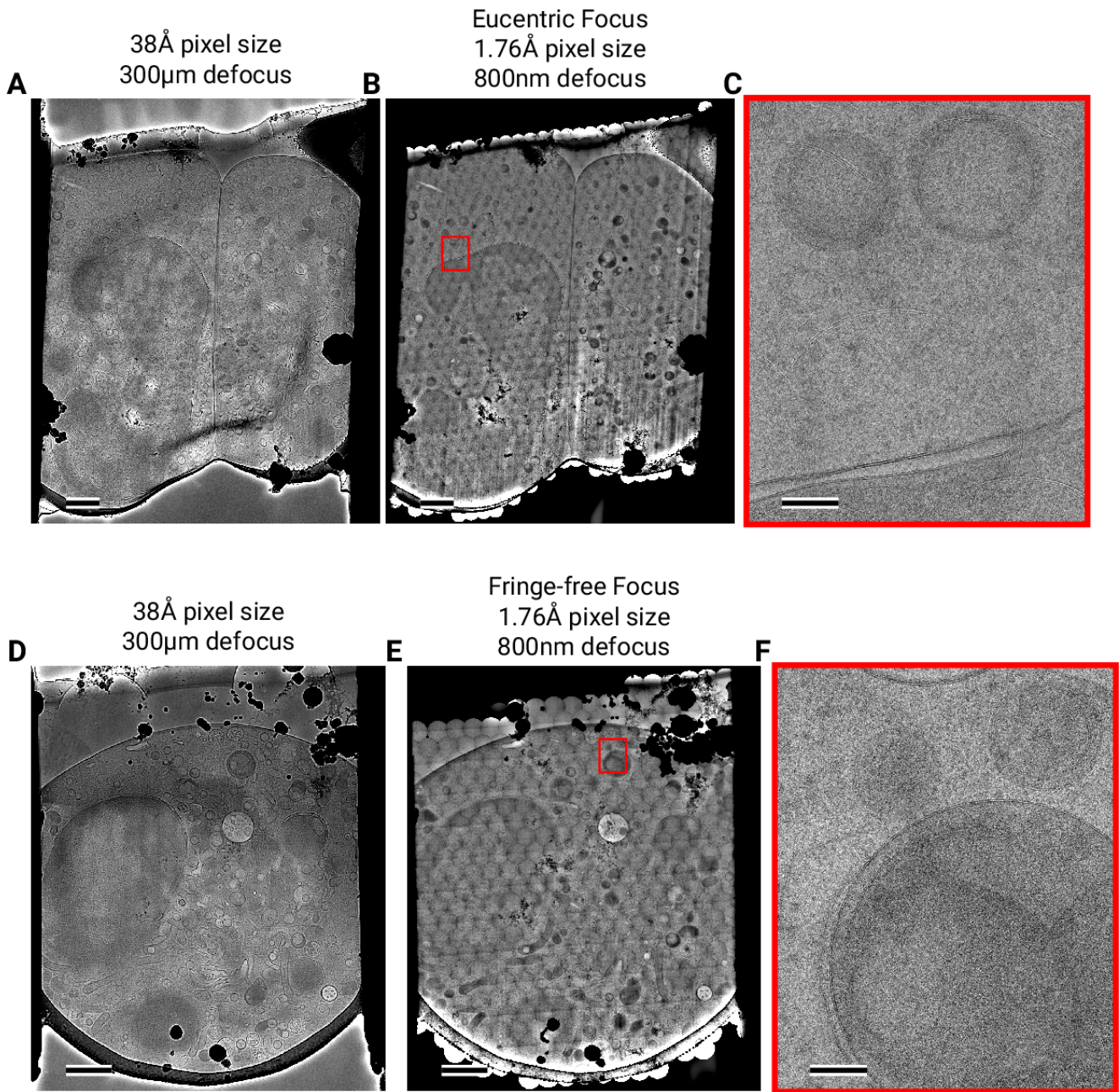


Figure 3: Assembling DeCo-LACE exposures into montages (A) Overview image of Lamella_{EUC} 1 taken at low magnification. Scalebar corresponds to 1 m. (B) Overview of Lamella_{EUC} 1 created by montaging high magnification images taken with the DeCo-Lace approach. Scalebar corresponds to 1 m. (C) Zoom-in into red box in panel B. Slight beam-fringe artifacts are visible. Scalebar corresponds to 100 nm. (D) Overview image of Lamella_{FFF} 4 taken at low magnification. Scalebar corresponds to 1 m. (E) Overview of Lamella_{FFF} 4 created by montaging high magnification images taken with the DeCo-Lace approach. Scalebar corresponds to 1 m. (F) Zoom-in into red box in panel E. No beam-fringe artifacts are visible. Scalebar corresponds to 100 nm.

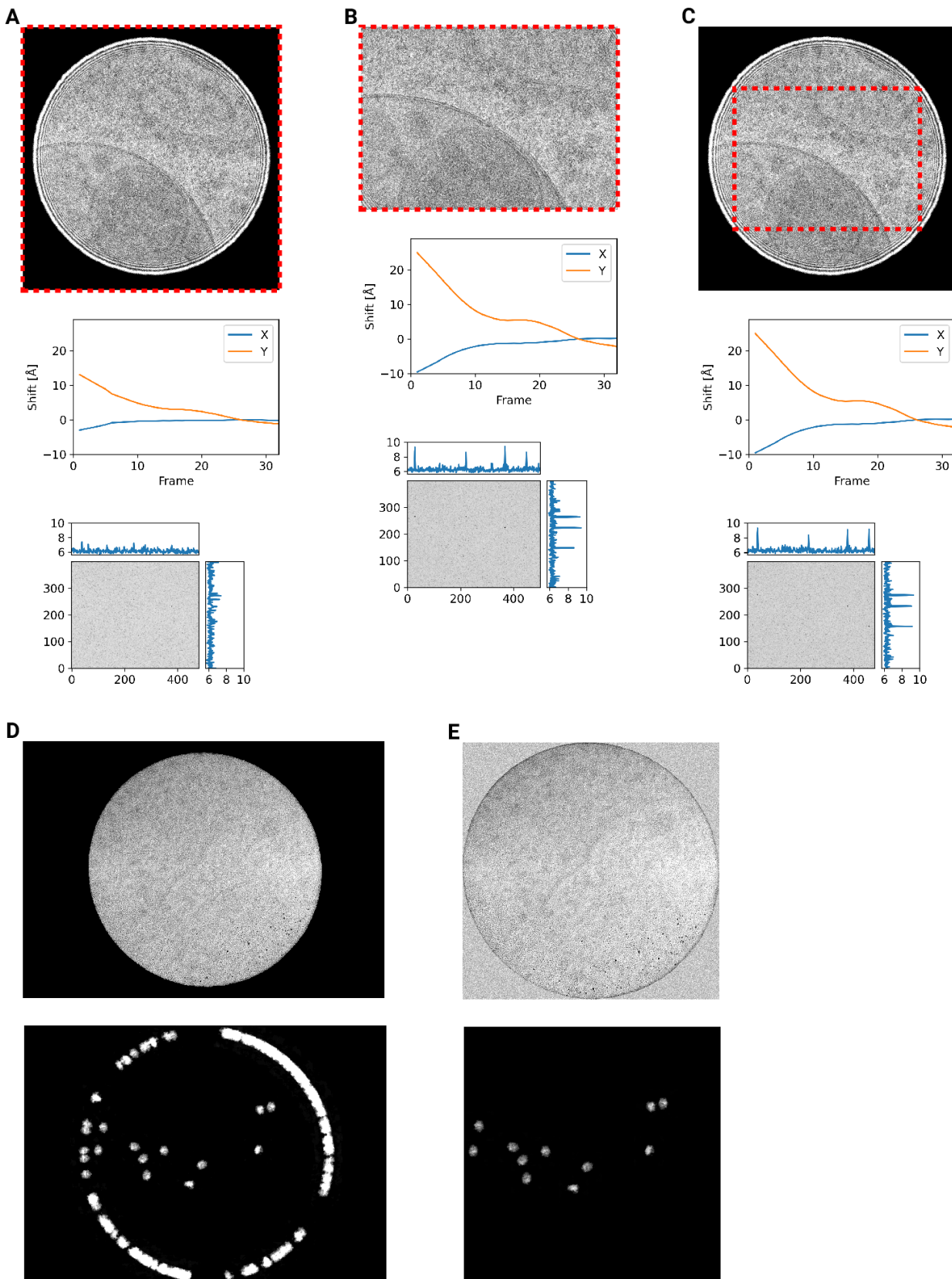


Figure 4 - figure supplement 1: Motion correction of movies with condensed beams. At the top of each panel is an average of the movie that was motion-corrected with a red dashed box indicating the region that was used to estimate shifts. Below is a graph indicating the estimated shifts of the individual frames of the movie. Below this is the MIP of 2DTM using the large subunit of the mouse ribosome. (A) Motion correction of the whole movie (B) Motion correction of a cropped region of the movie that eliminates the beam edges (C) Motion correction of the whole movie, using only the central region to estimate the shifts

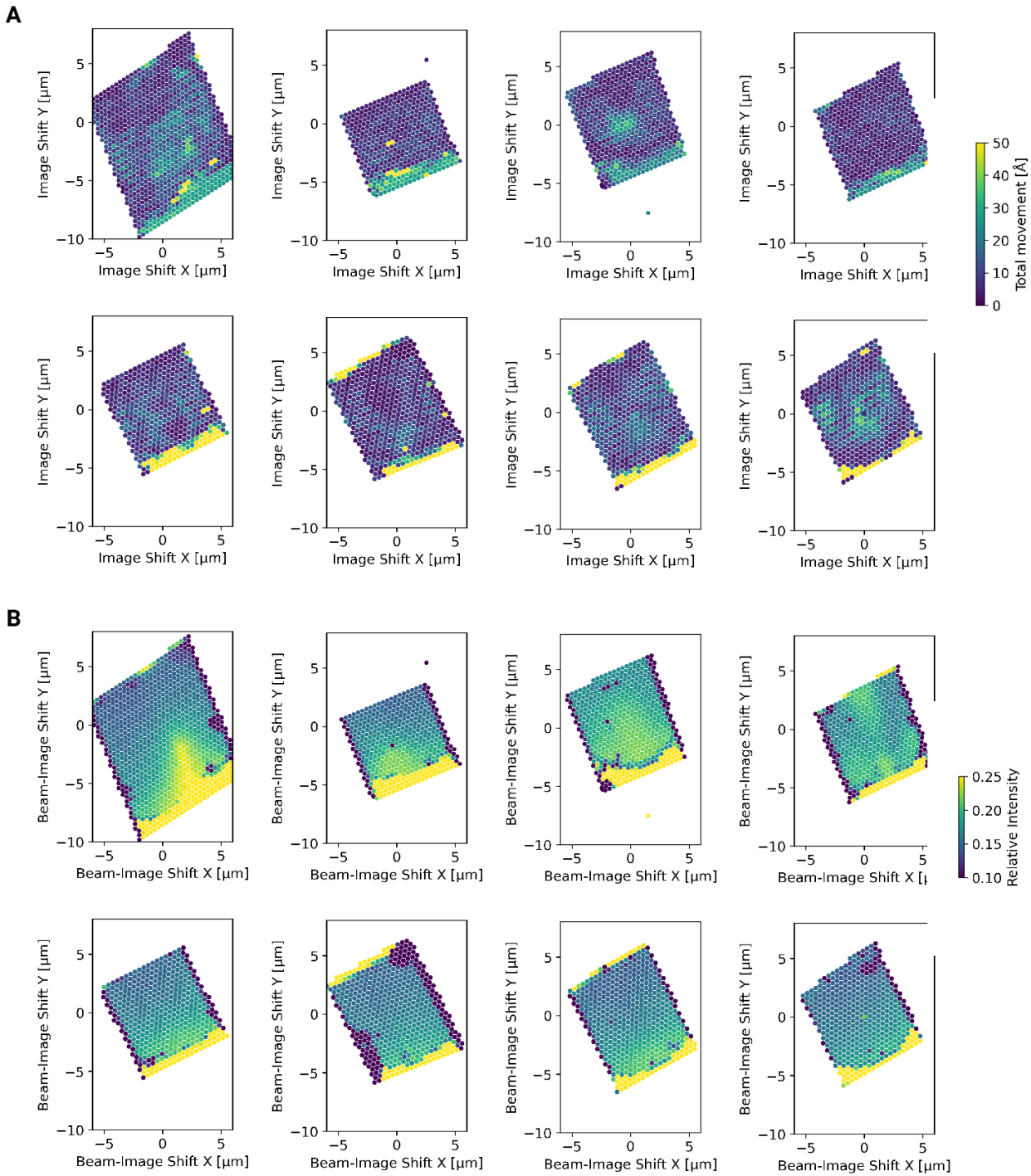


Figure 4 - figure supplement 2: Motion correction of individual tiles imaged using the DeCo-LACE approach (A) Total estimated motion of individual micrographs taken using the DeCo-Lace approach plotted as a function of the beam image-shift values. (B) Electron intensity of individual micrographs taken using the DeCo-Lace approach plotted as a function of the beam image-shift values.

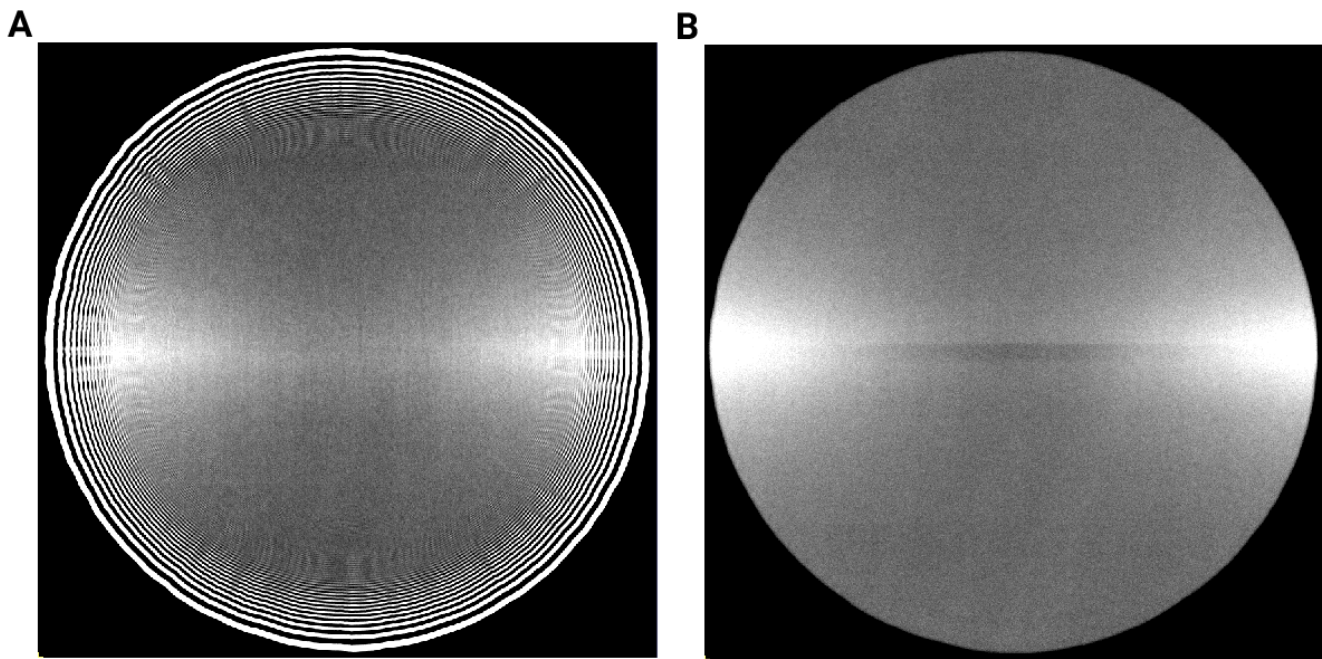


Figure 4 - figure supplement 3: Averages of micrographs taken with a condensed beam over vacuum using a Gatan K3 detector. Contrast and Brightness have been adjusted to highlight uneven dose response. (A) Eucentric Focus (B) Fringe-free Focus

³⁷² 1. **Label-free, normalized quantification of complex mass spectrometry data for proteomic analysis** Noelle M Griffin, Jingyi Yu, Fred Long, Phil Oh, Sabrina Shore, Yan Li, Jim A Koziol, Jan E Schnitzer

Nature Biotechnology (2010-01) <https://doi.org/fshgnc> DOI: 10.1038/nbt.1592 · PMID: 20010810 · PMCID: PMC2805705

³⁷³

³⁷⁴ 2. **Fluorescence microscopy** Jeff W Lichtman, José-Angel Conchello

Nature Methods (2005-11-18) <https://doi.org/bbpg4n> DOI: 10.1038/nmeth817 · PMID: 16299476

³⁷⁵

³⁷⁶ 3. **A visual approach to proteomics** Stephan Nickell, Christine Kofler, Andrew P Leis, Wolfgang Baumeister

Nature Reviews Molecular Cell Biology (2006-02-15) <https://doi.org/d6d5mq> DOI: 10.1038/nrm1861 · PMID: 16482091

³⁷⁷

³⁷⁸ 4. **Electron microscopy of frozen hydrated sections of vitreous ice and vitrified biological samples** AW McDowall, J-J Chang, R Freeman, J Lepault, CA Walter, J Dubochet

Journal of Microscopy (1983-07) <https://doi.org/bdnzmv> DOI: 10.1111/j.1365-2818.1983.tb04225.x · PMID: 6350598

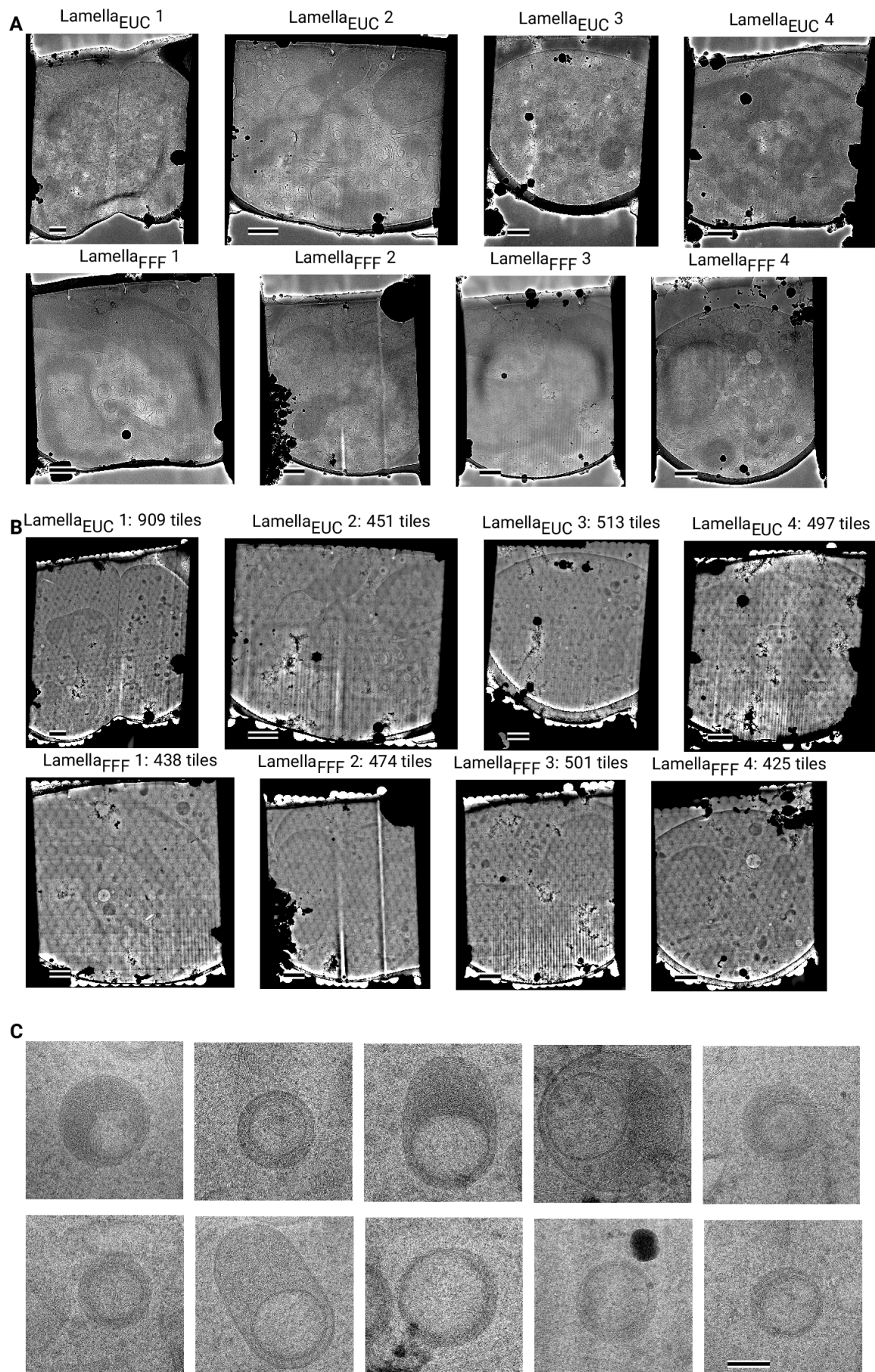


Figure 4 - figure supplement 4: Overview images of lamellae imaged using the DeCo-LACE approach taken at low-magnification (A) Overviews taken at low magnification.²¹ Scalebar corresponds to 1 m. (B) Overviews assembled using the DeCo-LACE approach. Scalebar corresponds to 1 m. (C) Representative examples of a class of granules containing a putatively cytosolic inclusion. Scalebar corresponds to 100 nm.

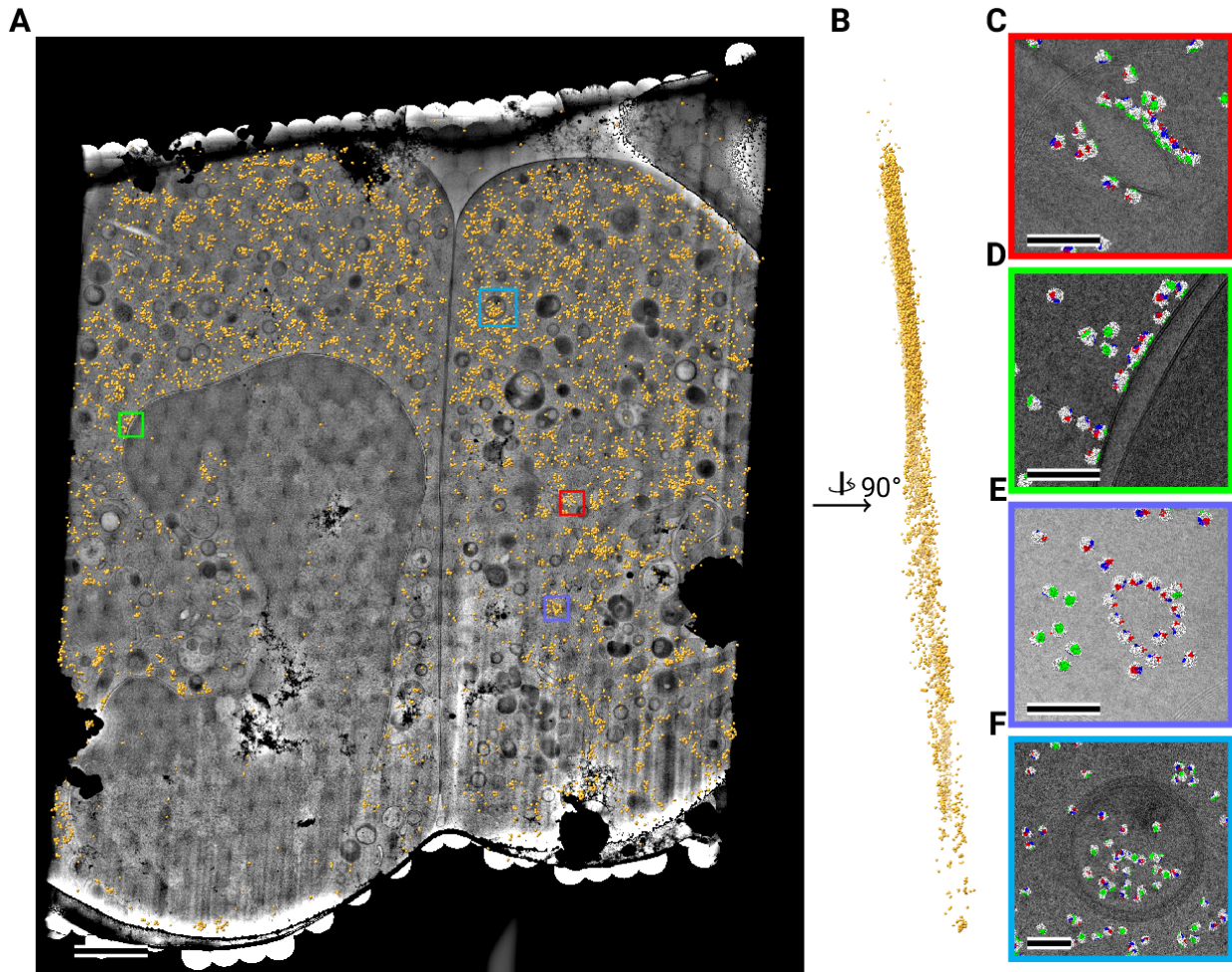


Figure 4: Template matching in lamella imaged using the DeCo-Lace approach at eucentric focus (A) Montage of Lamella_{EUC} 1 overlaid with detected targets colored in orange. Scalebar corresponds to 1 m. (B) Side view of detected targets in the lamella, such that the direction of the electron beam is horizontal. (C-F) Magnified area of panel A showing rough ER with associated ribosomes (C), outer nuclear membrane with associated ribosomes (D), ribosomes arranged in a circular fashion (E), ribosomes enclosed in a less electron dense inclusion in a granule (F). Ribosomes are colored in white with the surface of the peptide exit tunnel colored in green and the A, P, and E sites colored in blue, purple, and red, respectively. Scalebar corresponds to 100 nm.

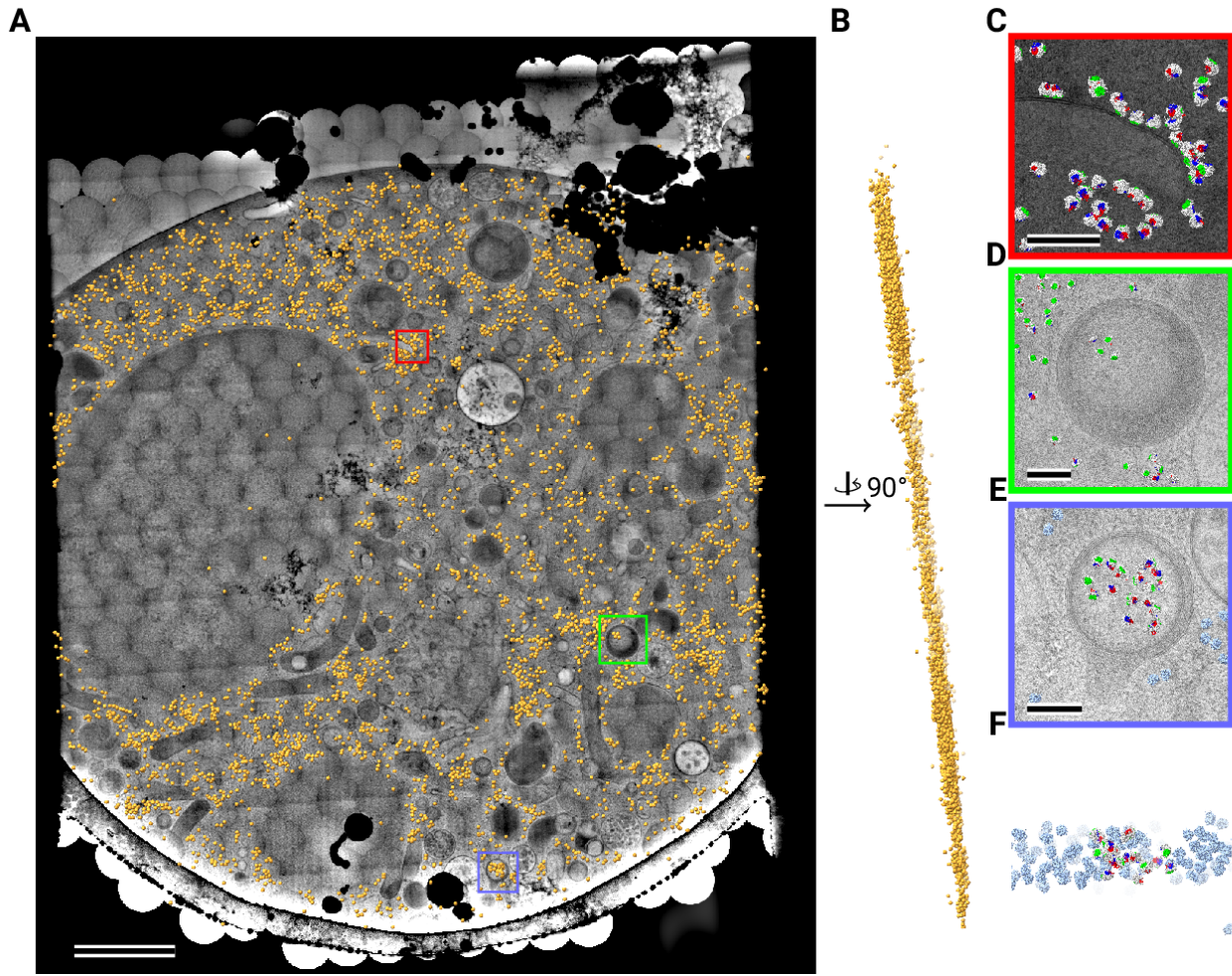


Figure 5: Template matching in lamella imaged using the DeCo-Lace approach (A) Montage of Lamella_{FFF} 4 overlaid with detected targets colored in orange. Scalebar corresponds to 1 m. (B) Side view of detected targets in the lamella, such that the direction of the electron beam is horizontal. (C-E) Magnified area of panel A showing rough ER with associated ribosomes (C) and ribosomes enclosed in a less electron dense inclusion in a granule (D,E). (F) Side view of panel E. Ribosomes are colored in white with the surface of the peptide exit tunnel colored in green and the A, P, and E sites colored in blue, purple, and red, respectively. Scalebar corresponds to 100 nm.

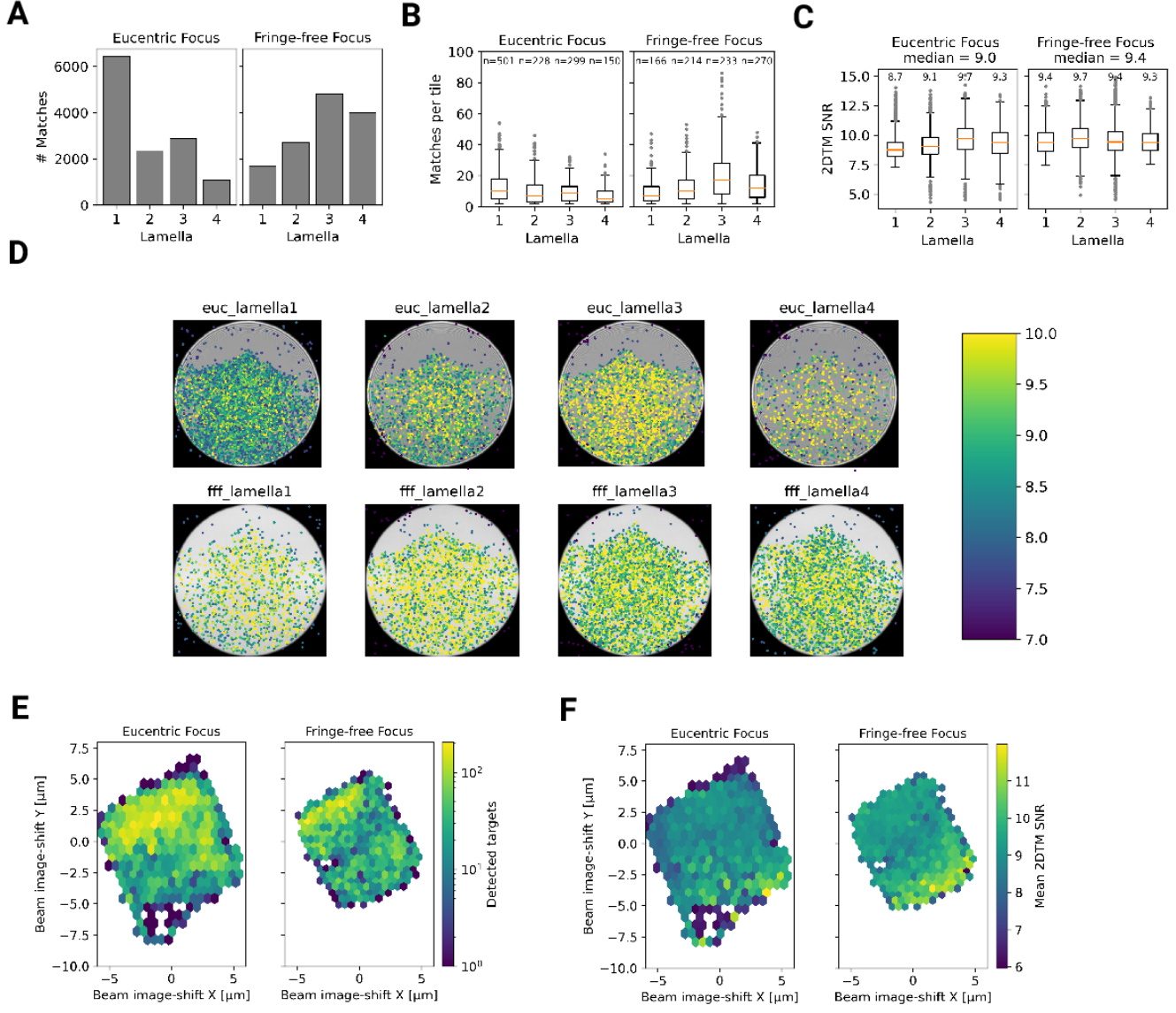


Figure 6: Statistics of 2DTM on lamella imaged using DeCo-LACE (A) Number of detected targets in each lamella (B) Distribution of targets per tile in each lamella. Only tiles with two or more detected targets were included (C) Distribution of SNRs in each lamella (D) For each lamella an average of all tiles is shown. Overlaid is a scatterplot of all detected targets in these tiles according to their in-tile coordinates. Scatterplot is colored according to the 2DTM SNR. There are no detected targets in the top circle-circle intersection due to radiation damage from previous exposures. (E) 2D histogram of number of detected targets as a function of beam-image shift (F) Mean 2DTM SNR as a function of beam-image shift

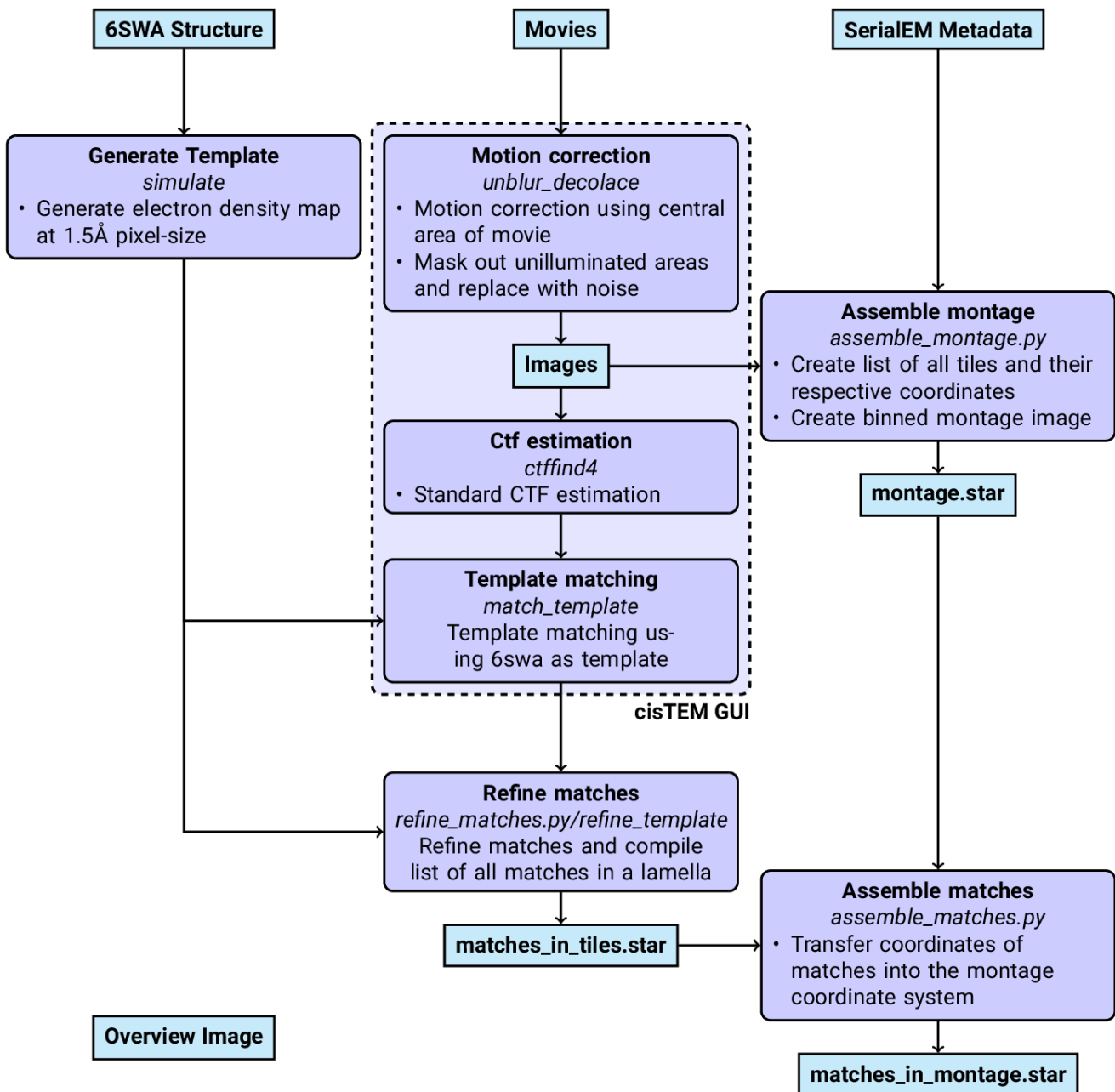


Figure 7: Workflow of DeCo-Lace processing

Figure Movie 1: Movie of detected LSU targets in Lamella_{EUC} 1, corresponding to Figure 5

Figure Movie 2: Movie of detected LSU targets in Lamella_{FFF} 4, corresponding to Figure 6

379

380 5. **Opening windows into the cell: focused-ion-beam milling for cryo-electron tomography**

Elizabeth Villa, Miroslava Schaffer, Jürgen M Plitzko, Wolfgang Baumeister

Current Opinion in Structural Biology (2013-10) <https://doi.org/f537jp> DOI: 10.1016/j.sbi.2013.08.006 ·

PMID: 24090931

381

382 6. **Electron tomography of cells** Lu Gan, Grant J Jensen

Quarterly Reviews of Biophysics (2011-11-15) <https://doi.org/czj9hr> DOI: 10.1017/s0033583511000102 ·

PMID: 22082691

383

384 7. **Single-protein detection in crowded molecular environments in cryo-EM images** JPeter Rick-

gauer, Nikolaus Grigorieff, Winfried Denk

eLife (2017-05-03) <https://doi.org/gnq4q4> DOI: 10.7554/elife.25648 · PMID: 28467302 · PMCID:

PMC5453696

385

386 8. **Label-free single-instance protein detection in vitrified cells** JPeter Rickgauer, Heejun Choi,

Jennifer Lippincott-Schwartz, Winfried Denk

Cold Spring Harbor Laboratory (2020-04-24) <https://doi.org/gpbjfd> DOI: 10.1101/2020.04.22.053868

387

388 9. **Locating macromolecular assemblies in cells by 2D template matching with cisTEM** Bronwyn

A Lucas, Benjamin A Himes, Liang Xue, Timothy Grant, Julia Mahamid, Nikolaus Grigorieff

eLife (2021-06-11) <https://doi.org/gkkc49> DOI: 10.7554/elife.68946 · PMID: 34114559 · PMCID:

PMC8219381

389

390 10. **Inhibition of Dihydroorotate Dehydrogenase Overcomes Differentiation Blockade in Acute**

Myeloid Leukemia David B Sykes, Youmna S Kfouri, François E Mercier, Mathias J Wawer, Jason M

Law, Mark K Haynes, Timothy A Lewis, Amir Schajnovitz, Esha Jain, Dongjun Lee, ... David T Scadden

Cell (2016-09) <https://doi.org/f3r5jr> DOI: 10.1016/j.cell.2016.08.057 · PMID: 27641501 · PMCID:

PMC7360335

391

392 11. **Hallmarks of ribosomopathies** Kim R Kampen, Sergey O Sulima, Stijn Vereecke, Kim De Keersmaecker

Nucleic Acids Research (2019-07-27) <https://doi.org/gpbjfm> DOI: 10.1093/nar/gkz637 · PMID: 31350888

· PMCID: PMC7026650

393

- 394 12. **Diagnostic and prognostic implications of ribosomal protein transcript expression patterns in**
human cancers James M Dolezal, Arie P Dash, Edward V Prochownik
BMC Cancer (2018-03-12) <https://doi.org/gc87j9> DOI: 10.1186/s12885-018-4178-z · PMID: 29530001 ·
PMCID: PMC5848553
- 395
- 396 13. **< i > In situ </ i > single particle classification reveals distinct 60S maturation intermediates in**
cells Bronwyn A Lucas, Kexin Zhang, Sarah Loerch, Nikolaus Grigorieff
Cold Spring Harbor Laboratory (2022-04-10) <https://doi.org/gp4qrw> DOI: 10.1101/2022.04.10.487797
- 397
- 398 14. **Protein Synthesis in the Developing Neocortex at Near-Atomic Resolution Reveals Ebp1-**
Mediated Neuronal Proteostasis at the 60S Tunnel Exit Matthew L Kraushar, Ferdinand Krupp,
Dermot Harnett, Paul Turko, Mateusz C Ambrozkiewicz, Thiemo Sprink, Koshi Imami, Manuel Gündig-
mann, Ulrike Zinnall, Carlos H Vieira-Vieira, ... Christian MT Spahn
Molecular Cell (2021-01) <https://doi.org/gh7d72> DOI: 10.1016/j.molcel.2020.11.037 · PMID: 33357414 ·
PMCID: PMC8163098
- 399
- 400 15. **Advances in Single Particle Analysis Data Acquisition** Stan Konings, Maarten Kuijper, Jeroen
Keizer, Fanis Grollios, Tjerk Spanjer, Peter Tiemeijer
Microscopy and Microanalysis (2019-08) <https://doi.org/gp9bqm> DOI: 10.1017/s1431927619005798
- 401
- 402 16. **High-quality, high-throughput cryo-electron microscopy data collection via beam tilt and**
astigmatism-free beam-image shift Chunling Wu, Xiaojun Huang, Jing Cheng, Dongjie Zhu, Xinzhen
Zhang
Journal of Structural Biology (2019-12) <https://doi.org/gp2nq9> DOI: 10.1016/j.jsb.2019.09.013 · PMID:
31562921
- 403
- 404 17. **THE DEVELOPMENT OF NEUTROPHILIC POLYMORPHONUCLEAR LEUKOCYTES**
IN HUMAN BONE MARROW Dorothy Ford Bainton, Joan L Ulliyot, Marilyn G Farquhar
Journal of Experimental Medicine (1971-10-01) <https://doi.org/chkbcm> DOI: 10.1084/jem.134.4.907 ·
PMID: 4106490 · PMCID: PMC2138991

405

- 406 18. **Routine determination of ice thickness for cryo-EM grids** William J Rice, Anchi Cheng, Alex J
Noble, Edward T Eng, Laura Y Kim, Bridget Carragher, Clinton S Potter
Journal of Structural Biology (2018-10) <https://doi.org/gfbpj2> DOI: 10.1016/j.jsb.2018.06.007 · PMID:
29981485 · PMCID: PMC6119488
- 407
- 408 19. **Optimized cryo-focused ion beam sample preparation aimed at in situ structural studies of
membrane proteins** Miroslava Schaffer, Julia Mahamid, Benjamin D Engel, Tim Laugks, Wolfgang
Baumeister, Jürgen M Plitzko
Journal of Structural Biology (2017-02) <https://doi.org/f9qfr6> DOI: 10.1016/j.jsb.2016.07.010 · PMID:
27444390
- 409
- 410 20. **Circularization of mRNA by eukaryotic translation initiation factors.** SE Wells, PE Hillner, RD
Vale, AB Sachs
Molecular cell (1998-07) <https://www.ncbi.nlm.nih.gov/pubmed/9702200> DOI: 10.1016/s1097-
2765(00)80122-7 · PMID: 9702200
- 411
- 412 21. **Montage electron tomography of vitrified specimens** Ariana Peck, Stephen D Carter, Huanghao
Mai, Songye Chen, Alister Burt, Grant J Jensen
Journal of Structural Biology (2022-06) <https://doi.org/gp4qrs> DOI: 10.1016/j.jsb.2022.107860 · PMID:
35487464
- 413
- 414 22. **Correlative cryogenic montage electron tomography for comprehensive in-situ whole-cell
structural studies** Jie E Yang, Matthew R Larson, Bryan S Sibert, Joseph Y Kim, Daniel Parrell, Juan C
Sanchez, Victoria Pappas, Anil Kumar, Kai Cai, Keith Thompson, Elizabeth R Wright
Cold Spring Harbor Laboratory (2022-01-02) <https://doi.org/gp4qrw> DOI: 10.1101/2021.12.31.474669
- 415
- 416 23. **Beam image-shift accelerated data acquisition for near-atomic resolution single-particle cryo-
electron tomography** Jonathan Bouvette, Hsuan-Fu Liu, Xiaochen Du, Ye Zhou, Andrew P Sikkema,
Juliana da Fonseca Rezende e Mello, Bradley P Klemm, Rick Huang, Roel M Schaaper, Mario J Borgnia,
Alberto Bartesaghi
Nature Communications (2021-03-30) <https://doi.org/gjphkb> DOI: 10.1038/s41467-021-22251-8 · PMID:
33785757 · PMCID: PMC8009872

- 418 24. **Parallel cryo electron tomography on < i>in situ</i> lamellae** Fabian Eisenstein, Haruaki Yanagisawa, Hiroka Kashihara, Masahide Kikkawa, Sachiko Tsukita, Radostin Danev
Cold Spring Harbor Laboratory (2022-04-08) <https://doi.org/gp4qrw> DOI: 10.1101/2022.04.07.487557
- 419
- 420 25. **Waffle Method: A general and flexible approach for improving throughput in FIB-milling**
Kotaro Kelley, Ashleigh M Raczkowski, Oleg Klykov, Pattana Jaroenlak, Daija Bobe, Mykhailo Kopylov, Edward T Eng, Gira Bhabha, Clinton S Potter, Bridget Carragher, Alex J Noble
Nature Communications (2022-04-06) <https://doi.org/gp4qrt> DOI: 10.1038/s41467-022-29501-3 · PMID: 35387991 · PMCID: PMC8987090
- 421
- 422 26. **High-resolution cryo-EM using beam-image shift at 200 keV** Jennifer N Cash, Sarah Kearns, Yilai Li, Michael A Cianfrocco
IUCrJ (2020-10-29) <https://doi.org/gjwcfq> DOI: 10.1107/s2052252520013482 · PMID: 33209328 · PMCID: PMC7642776
- 423
- 424 27. **Shedding light on the cell biology of extracellular vesicles** Guillaume van Niel, Gisela D'Angelo, Graça Raposo
Nature Reviews Molecular Cell Biology (2018-01-17) <https://doi.org/gct4df> DOI: 10.1038/nrm.2017.125 · PMID: 29339798
- 425
- 426 28. **Exosome-mediated transfer of mRNAs and microRNAs is a novel mechanism of genetic exchange between cells** Hadi Valadi, Karin Ekström, Apostolos Bossios, Margareta Sjöstrand, James J Lee, Jan O Lötvall
Nature Cell Biology (2007-05-07) <https://doi.org/d5df4s> DOI: 10.1038/ncb1596 · PMID: 17486113
- 427
- 428 29. **Automated electron microscope tomography using robust prediction of specimen movements**
David N Mastronarde
Journal of Structural Biology (2005-10) <https://doi.org/ff7gzx> DOI: 10.1016/j.jsb.2005.07.007 · PMID: 16182563
- 429

- 430 30. **cisTEM, user-friendly software for single-particle image processing** Timothy Grant, Alexis Rohou, Nikolaus Grigorieff
eLife (2018-03-07) <https://doi.org/gf5cq7> DOI: 10.7554/elife.35383 · PMID: 29513216 · PMCID: PMC5854467
- 431
- 432 31. **Measuring the optimal exposure for single particle cryo-EM using a 2.6 Å reconstruction of rotavirus VP6** Timothy Grant, Nikolaus Grigorieff
eLife (2015-05-29) <https://doi.org/gf5cm7> DOI: 10.7554/elife.06980 · PMID: 26023829 · PMCID: PMC4471936
- 433
- 434 32. **CTFFIND4: Fast and accurate defocus estimation from electron micrographs** Alexis Rohou, Nikolaus Grigorieff
Journal of Structural Biology (2015-11) <https://doi.org/f7xzgv> DOI: 10.1016/j.jsb.2015.08.008 · PMID: 26278980 · PMCID: PMC6760662
- 435
- 436 33. **Cryo-TEM simulations of amorphous radiation-sensitive samples using multislice wave propagation** Benjamin Himes, Nikolaus Grigorieff
IUCrJ (2021-09-30) <https://doi.org/gpzs9r> DOI: 10.1107/s2052252521008538 · PMID: 34804546 · PMCID: PMC8562658
- 437
- 438 34. **scikit-image: image processing in Python** Stéfan van der Walt, Johannes L Schönberger, Juan Nunez-Iglesias, François Boulogne, Joshua D Warner, Neil Yager, Emmanuelle Gouillart, Tony Yu
PeerJ (2014-06-19) <https://doi.org/gftp3s> DOI: 10.7717/peerj.453 · PMID: 25024921 · PMCID: PMC4081273
- 439
- 440 35. **SciPy 1.0: fundamental algorithms for scientific computing in Python** Pauli Virtanen, Ralf Gommers, Travis E Oliphant, Matt Haberland, Tyler Reddy, David Cournapeau, Evgeni Burovski, Pearu Peterson, Warren Weckesser, Jonathan Bright, ...
Nature Methods (2020-02-03) <https://doi.org/ggj45f> DOI: 10.1038/s41592-019-0686-2 · PMID: 32015543 · PMCID: PMC7056644

⁴⁴² 36. <scp>UCSF ChimeraX</scp> : Structure visualization for researchers, educators, and developers Eric F Pettersen, Thomas D Goddard, Conrad C Huang, Elaine C Meng, Gregory S Couch, Tristan I Croll, John H Morris, Thomas E Ferrin

Protein Science (2020-10-22) <https://doi.org/ghr6mn> DOI: 10.1002/pro.3943 · PMID: 32881101 · PMCID: PMC7737788

⁴⁴³